An X-ray micro-tomographic study of the pore space, permeability and percolation threshold of young sea ice

Sönke Maus[1], Martin Schneebeli[2], and Andreas Wiegmann[3]

[1]Department of Civil and Environmental Engineering, NTNU, Trondheim, NORWAY
[2]WSL Swiss Federal Institute for Snow and Avalanche Research, Davos, SWITZERLAND
[3]Math2Market GmbH, Kaiserslautern, GERMANY

Correspondence: Sönke Maus (sonke.maus@ntnu.no)

Abstract. The hydraulic permeability of sea ice is an important property that influences the role of sea ice in the environment in many ways. As it is difficult to measure, so far not many observations exist and the quality of deduced empirical relationships between porosity and permeability is unknown. The present work presents a study of the permeability of young sea ice based on the combination of X-ray tomographic imaging and direct numerical simulations. The approach is new for sea ice. It allows

5 to relate the permeability and percolation properties explicitly to characteristic properties of the sea ice pore space, in particular to pore size and connectivity metrics. For the young ice from the present field study we obtain a brine volume of 2.4 ± 0.3 % as threshold for the vertical permeability (transition to impermeable sea ice). We are able to relate this transition to the necking of brine pores at a critical pore throat diameter of ≈ 0.07 mm, being consistent with some limited pore analysis from earlier studies. The obtained critical brine porosity is considerably smaller than the value of 5 % proposed in earlier work and frequently adopted in sea ice model studies and applications. We revise the uncertainties associated with earlier estimates

10 suggesting that the present result is more accurate. We then propose a consistent parametrisation for the permeability of young sea ice that will be useful for modelling. The study highlights the large potential of X-ray tomography, in combination with appropriate sampling, storage and processing, to derive physical properties of sea ice.

1 Introduction

15 Sea ice is a porous medium that covers, on average, 5 to 7 percent of the earth's oceans. To understand the role of sea ice in the earth system, its hydraulic permeability needs to be known. A proper understanding of the salinity evolution of sea ice requires the knowledge of its permeability (Cox and Weeks, 1988; Worster and Wettlaufer, 1997; Petrich et al., 2006; Vancoppenolle et al., 2007; Wells et al., 2013; Griewank and Notz, 2013; Turner et al., 2013; Rees Jones and Grae Worster, 2014). Through its control of the salinity of sea ice, the permeability furthermore impacts the evolution of many other physical properties like

20 like sea ice strength and and thermal conductivity (Cox and Weeks, 1988; Worster and Wettlaufer, 1997), that depend on the brine porosity of sea ice. Of high relevance for sea ice in the climate system is also the role of permeability for the *Melt pond albedo feedback*: Melt ponds from melted snow, appearing on sea ice during summer, will drain when the sea ice is permeable, exposing an ice surface that reflects more sunlight than ponded ice (e.g., Freitag and Eicken, 2003).

While permeability plays a key role for proper modelling and understanding of sea ice properties, observations are sparse and span, even at a fixed porosity, 2-3 orders of magnitude (Maksym and Jeffries, 2000). Test procedures used so far all suffer from shortcomings. Field measurements based on the filling rate of in situ boreholes only give some average measure of near-bottom permeability. These values further depend on the unknown permeability anisotropy and pore space details, and thus are uncertain (Freitag, 1999; Freitag and Eicken, 2003; Golden et al., 2007). Laboratory studies have been restricted to relatively young and thin ice (Saito and Ono, 1978; Ono and Kasai, 1985; Saeki et al., 1986; Okada et al., 1999). To what degree these experiments resemble natural sea ice is uncertain and may only be answered by a comparison of microstructure and pore scales, not performed so far. The most frequently cited study of sea ice permeability (Freitag, 1999) was based on samples from an ice tank experiment. Ice core segments were first centrifuged at in situ temperatures, before the permeability was obtained experimentally with a kerosin-based permeameter setup. The advantage of centrifuging ice samples and using a liquid that does not mix with water is to avoid microstructure changes that inevitably take place during storage and/or fluid flow. However, since the study by Freitag (1999) no further observations to validate the permeability values based on this method have been published. It is thus unclear, to what degree the results are valid for natural sea ice, and how different ice growth and age might affect the results.

The present study follows the centrifuging approach by Freitag (1999) and extends it in several ways. First, the permeability of centrifuged sea ice samples is not determined by a laboratory permeameter, but through direct numerical simulations on 3D X-ray microtomographic (XRT) images. Second, we perform a statistical analysis of the 3D XRT-based pore space that allows for a physical interpretation of permeability in terms of pore sizes and connectivity. Third, we extend the so far documented porosity range to values when the ice becomes impermeable, obtain an estimate of the threshold porosity, and analyse the pore space near the threshold. Our approach allows us to revise the percolation threshold of $\phi \approx 0.05$ that has been proposed in earlier studies without consideration of the micro-structural pore size details (Petrich et al., 2006; Golden et al., 2007). Furthermore, we present a relationship between permeability and brine porosity that is valid over a wider range of porosities than so far investigated.

2 Field work and methods

2.1 Field sampling

Sea ice samples for the present study were obtained from fast ice in Adventbay of Adventfjorden, Svalbard during 14th to 19th April 2011, approximately 2 km from the UNIS (University Courses on Svalbard) building (Figure 1). The meteorological conditions indicate, in combination with daily ice charts from the Ice service of the Norwegian Meteorological Institute (ftp.met.no/pub/icecharts/, not shown), that the ice was approximately 3-4 weeks old. After, most likely, freeze-up during 20.-22.04.2011, it mostly grew during a period of 10 days with temperatures around -20 °C, followed by 10 days with gradual warming. A 10 cm cover of new snow on the ice had mostly accumulated a few days prior to sampling.

During each sampling date 6 full ice cores were obtained with a 7.25 cm diameter coring device (Mark III, Kovacs Enterprises) from 35 cm thick fast ice. Cores were immediately cut into 3-4 cm thick subsamples. On a first ice core, temperatures
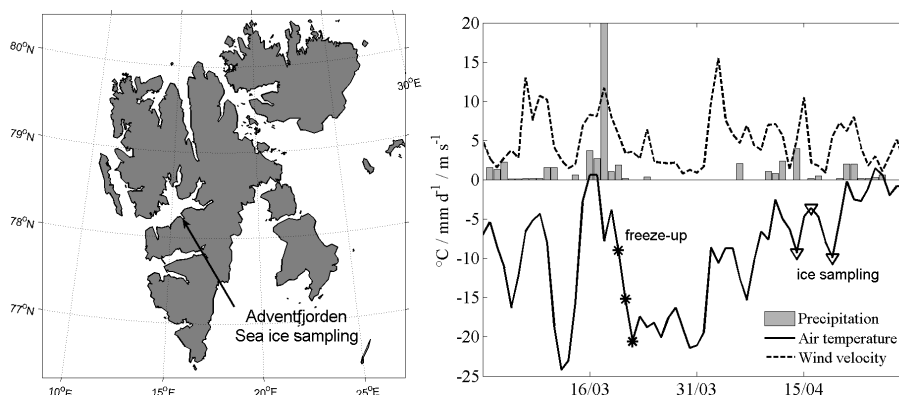
Figure 1. Left: Location of sampling of young sea ice in Adventbay/Adventfjorden. Right: Meteorological conditions at Longyearbyen airport in March/April 2011, from freeze-up ($*$) to sampling three to four weeks later ($\triangledown$)

were measured with a penetration probe - this core was not used further. All other core segments were packed in plastic beakers, stored in an isolating box and rapidly (by snow mobiles, within 30 minutes from the beginning of coring) transported to the UNIS laboratory. Here they were moved into temperature-controlled freezers (WAECO Coolfreeze T56) close to their *in situ*

60   temperatures (typically within 0.3 K). During the three sampling dates a total of 15 ice cores were obtained and sectioned into 145 subsamples.

2.2 Laboratory cooling sequence

In situ sea ice temperatures were in the range -2 to -3 °C. To extend this natural range we used the following approach in the laboratory. For each of the three sampling dates one core was left at *in situ* temperatures. The sub samples from the 4 replicate

65   cores were put into freezers controlled at lower temperatures -3, -4, -6, -8 and -10 °C and equilibrated by 1 to 3 days. The result is, for each level in the ice, a series of 5 samples with temperatures gradually ranging between in situ values (-2 to -3 °C) and minimum temperatures in the range -8 to -10 °C. In this way we generate samples with up to 4.5 times smaller brine porosity compared to the *in situ* condition.

2.3 Centrifugation

70   In a laboratory at UNIS the subsamples were centrifuged in a refrigerated centrifuge (Sigma 6K15). In our protocol the subsamples were placed on the field site into conical buckets to collect the brine that drained from them during storage. Centrifuging was performed 1 to 4 days after sampling, with longer waiting time for those samples cooled to lower temperatures. To do so, samples were placed into flexible stainless steel tea-sieves that fitted into the conical plastic buckets. Centrifuging thus extracted the brine from brine channels with a downward orientation and open to the bottom or perimeter of the sub-sample.

75   Centrifuging was performed at *in situ* temperatures (one core), and at the lowered temperatures from the sequence (4 cores). The centrifuged ice samples were, immediately after centrifugation set into a -80 °C freezer. On the next the mass of centrifuged

brine and residual ice samples was measured. The centrifuged samples were then cut down from the initial 7.25 cm to 3.5 cm diameter, and the ice that was cut off was melted. The centrifuged brine and melted residual ice were filtered with a 100 μm sieve, before the salinity was determined via measurements of the electrolytic conductivity and temperature (instrument WTW

80 Cond 340i). Brine samples with salinity > 40 g/kg were diluted to perform the conductivity-salinity conversion with seawater standard formulas. Salinity values obtained in this way have an accuracy of better than 0.2 g/kg.

A duration of 15 minutes and a centrifuge acceleration of $40 \times g$ (earth gravity) was selected for centrifuging. These numbers have been chosen due to several aspects of the approach. The acceleration ensures a pressure force ($40\rho_i gH$) of less than 15 kPa, well below the lowest tensile strength values (20-50 kPa) observed for natural sea ice (Weeks, 2010). This ensures that

85 samples do not deform internally during centrifuging, though it could not prevent the compression and micro-fracture of the fragile ice-seawater interface sub-sample. Second, it is important to set the centrifuge temperature close to but slightly (0.5-1 K) below the sample temperature, because otherwise the samples may warm up in the end and release additional brine. A third aspect, the impact of parameter choice on proper brine removal, is discussed below in connection with the permeability simulations.

90 As discussed in earlier applications (Weissenberger et al., 1992; Freitag, 1999; Krembs et al., 2001) centrifuging gives important information about the disconnected and connected fractions of the brine pore space. The centrifuged porosity may be associated with the *effective porosity* ϕ_{eff} relevant for fluid flow/permeability (Freitag, 1999), for which we shall use ϕ_{en} henceforth. Let the total brine porosity ϕ be the sum of the centrifuged brine porosity ϕ_{cen} and the residual brine porosity ϕ_{res}. Assuming that the corresponding brine salinities are the same, these porosities may be determined from salinity determinations

95 alone:

$$\phi_{cen} = 1 - \phi \frac{S_{ir}}{S_i} \left(\frac{S_b - S_i}{S_b - S_{ir}} \right), \quad \phi_{res} = \phi_b - \phi_{cen} \tag{1}$$

where S_i is the bulk salinity of the original ice sample, S_{ir} the residual salinity of a sample after centrifugation and S_b the salinity of the centrifuged brine, and ϕ was determined from S_i and temperature T_i, assuming thermodynamic equilibrium and applying equations from Cox and Weeks (1983).[1].

100 The centrifuged and cut ice samples were further stored in a -80 °C low temperature freezer, and and kept for 2 months at this temperature (including transport on dry ice). 2 days prior to imaging by X-ray micro-computed tomography (XRT) described below the samples were equilibrated to -20 °C.

2.4 X-ray micro-tomography

X-ray tomographic imaging was performed at the WSL Swiss Federal Institute for Snow and Avalanche Research, Davos,

105 Switzerland, with two desktop cone-beam microCT instruments (MicroCT 40 and MicroCT 80, Scanco Medical AG) that operate with a microfocus X-ray source (7 μm diameter) and detectors of 2048 x 256 and 2048 x 128 elements, respectively. The instrument was located in a cold room at -20 °C. However, the temperature within the CT chamber was slightly higher, -16 °C.

---

[1]Alternatively ϕ_{cen} and ϕ_{res} can be computed from the mass and salinity of the centrifuged brine and ice samples (Weissenberger et al., 1992)
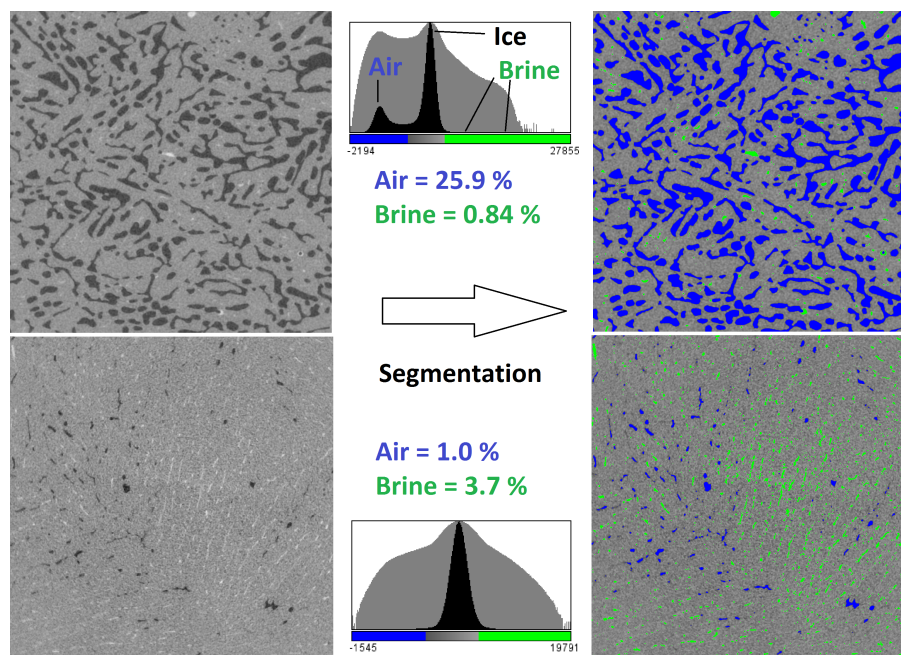
Figure 2. Segmentation of pre-filtered grey scale absorption images (left) into the classes of air (blue), brine (green) and ice (grey) for a high porosity (upper) and low porosity (lower) image. The images in the middle give the histograms of grey values with a linear (black) and a log (grey) scale. Upper example: a high porosity image with a well-defined air peak, yet little entrapped brine. Lower example: a sample with more entrapped brine than air/centrifuged brine.

The samples, after centrifugation reduced to 35 mm diameter, were again slightly reduced to fit into the 35 mm diameter sample holders, and then scanned with a 37 mm field of view, yielding a nominal pixel size of $\approx 37000/2048 = 18\mu$m. Scanning time

110 was roughly 1 hour per centimetre sample height, and thus 3-4 hours per sub sample. 1000 images per 360 degrees rotation were obtained. For the image analysis. horizontally 1200 x 1200 pixels were cropped from the center of the 2048 x 2048 field of view, and 1500 pixels vertically. The resulting XRT grayscale images were stored as 16-bit stacks, and filtered with ImageJ (rsb.info.nih.gov/ij/), applying a 2 pixel median and Gaussian blur filter (standard deviation 1.5).

The image segmentation into air, ice and brine was also performed with ImageJ as illustrated in Figure 2 for two samples,

115 one with high air and low residual brine porosity and another one with low air and moderate brine porosity. Our approach to find the air-ice and ice-brine thresholds was as follows. First, brine was ignored, and a global threshold that separates air and ice was found on sub-images with approximately equal fractions of air pores and ice, using Otsu's method (Otsu, 1979). Comparison with manual segmentation of single thresholds indicates an accuracy of 0.5 to 1% for the air porosity, being higher at high porosities. For the ice-brine threshold it was more difficult to find an automated procedure. Segmentation with Otsu's

120 algorithm gave generally too high brine content (compared to direct measurements). The best results, comparing to measured salinity, were obtained within ImageJ using the so called Triangle algorithm, yet still with considerable scatter. It was thus decided to rather use an empirical approach that sets the ice-brine threshold to 1.20 times the grey value of the ice mode. This

number led to least deviation of average CT-derived salinity and the salinity of melted samples. However, also here the absolute uncertainty of brine volume was 0.5 to 1%, corresponding to a relative uncertainty of $30 - 100\%$, as residual brine porosities at -16 °C were low. Hence, the relative accuracy in residual brine determination is much smaller than for the air porosity. As most likely explanation it is considered that brine inclusions were not much larger than the voxel size, and that brine is often found together with tiny air bubbles. This implies a considerable number of mixed air-brine pixels that have a grey value just a bit larger than ice.

Hence, for the present pore sizes, spatial resolution and brine salinity (≈ 185 g/kg at -16°C) there are considerable uncertainties in ice-brine segmentation, and an unsupervised approach (i.e. without setting a threshold based on alternative bulk salinity measurements) was not found. However, the permeability is little or not affected by the residual brine, and rather relates to the open air porosity (centrifuged, connected brine) that was determined with reasonable accuracy.

The imaged samples, cylinders with 35 mm diameter and 25-30 mm height, were again subdivided vertically into samples of 5.5 mm height. The subdivision is important for proper determination of permeability and percolation, as for 20 mm high samples a considerable fraction (10-30%) of slightly (10 to 30 degrees) inclined pores are running off at the vertical sides. Examples of these 3D sub-images to be analysed here are shown in the sections below.

2.5 Permeability simulations

Flow through porous media at relatively low velocities is governed by Darcy's equation (Dullien, 1991; Nield and Bejan, 1999). In one dimension

$$\overline{V} = \frac{K}{\mu}\frac{dP}{dz}, \tag{2}$$

gives the dependence of average velocity $\overline{V}$ (discharge per unit area) on pressure gradient dP/dz, dynamic viscosity μ of the fluid and permeability K. The latter has dimensions of area and may be imagined as the cross section of an equivalent channel of fluid flow through the pore space. The present approach to obtain K is to centrifuge the brine from the pore space, store the samples, and later perform permeability experiments (Freitag, 1999) or CFD simulations (Maus et al., 2013). It is thus of interest how the settings during centrifuging may impact the results: Consider the hydrostatic pressure gradient $dP/dz = \rho_b g$ across a sample filled with brine of density ρ_b. Inserting this into Equation. 2 one obtains the relationship

$$\overline{V} = K\frac{g}{\nu}, \tag{3}$$

where the kinematic viscosity ν has replaced μ/ρ_b. This equation actually states the conversion from hydraulic permeability K to hydraulic conductivity $\overline{V}$. Replacing this bulk flow $\overline{V}$ by $\phi_{eff}V$, where V is the actual velocity within pores contributing to the flow, the condition for brine removal from a sample of height H during time t requires $\overline{V} > \phi_{eff}H/t$. Further replacing g by the effective g_{eff} in the centrifuge, we can write Equation. 3 as

$$K > \phi_{eff}\frac{H}{t}\frac{\nu}{g_{eff}}, \tag{4}$$

as condition for full removal of brine during centrifuging. With $\phi_{eff} = \phi = 0.024$ at the lower end of our porosity range (see below), sample thickness H=0.04 m, centrifugal time t = 9000 s, $\nu = 3.2 \times 10^{-4}$ m^{2}s^{-1} (at -10 °C) into Equation. 3, and

155 $g_{eff} = 40g$, we obtain $K > 9 \times 10^{-15} m^2$. In ice samples with a lower permeability one can expect incomplete removal of brine that will freeze during cooling, which may render the sample impermeable. As we will find below, the lowest simulated permeability value in our study is $8.1 \times 10^{-15} m^2$, close to the latter estimate. However, below we also find that ϕ_{eff} is much lower than ϕ when low porosities are approached, decreasing this limit for K by at least a factor of 3-4. We thus assume that insufficient brine removal during centrifuge acceleration is not not a large problem for our results.

160   Here we report on vertical permeability computations that have been performed with GeoDict "Geometric Material Models and Computational PreDictions of Material Properties" GeoDict (2012-2020). The simulations were run on the mentioned sub-images of 1200 x 1200 x 300 voxels (300 corresponds to 5.5 mm height), with the SimpleFFT solver of the FlowDict module in GeoDict. The solver obtains, for a given pressure drop across the sample, the stationary fluid flow on a uniform grid based on the iterative solution of the Stokes-Brinkman equation (Wiegmann, 2007; Cheng et al., 2013; Linden et al., 2018). Recent

165 work has demonstrated the quality of the numerical solution of the FlowDict solver in comparison to observations (Zermatten et al., 2011; Gervais et al., 2015; Gelb et al., 2019). In our setup a 10 pixels thick inflow region at the top and bottom of the sample was used in connection with periodic boundary conditions. Computations on 3D images of dimension 300 x 1200 x 1200 ($\approx$ 5.5 x 22 x 22 mm) required typically 25-30 GB RAM. Limiting the accuracy to 1% appeared to be sufficient for most samples to converge in between 200 to 600 iterations, which took typically 1 to 3 days per sample on a 4 core pc with a 3 GHz

170 CPU. Simulations performed for 150 images have been published (Maus et al., 2013). The latter results have been revised in the present study and simulations have been repeated for those samples that had not reached the convergence criterium (mostly low porosity/permeability samples). With currently faster hardware, and improvement of the Geodict solver, simulations are nowadays 10 to 20 times faster.

2.6 Pore space analysis

175 The permeability K of a porous medium (equation 2) is often parametrised in terms of total porosity in the form $K \sim \phi^b$, where the range $2 < b < 5$ has been found in observations (Dullien, 1991; Happel and Brenner, 1986). A more concise and physically consistent formula for the permeability is (Paterson, 1983, e.g.,)

$$K = a\tau^2 D_c^2 \phi_{eff}^b \qquad (5)$$

    wherein ϕ_{eff} is the effective porosity for fluid flow, D_c a characteristic pore diameter, τ tortuosity of the flow path and a

180 a constant. For simple flow geometries this relationship is exactly known. E.g., for a bundle of parallel cylindrical pores of diameter D_c with cross sectional area $\phi = \phi_{eff}$ one has $\tau = 1$ and $a = 1/32$, while a system of parallel vertical lammellae (flow through slits of width D) with $\phi = \phi_{eff}$ one has $a = 1/12$ (Paterson, 1983; Dullien, 1991, e.g.,). In more complex networks with a distribution of pore sizes one has to find a characteristic pore scale D, tortuosity τ and a will depend on the detailed network morphology. Here we shall investigating how D, τ and ϕ_{eff} all depend on total porosity, to understand for

185 which regime a simplified relationship $K \sim \phi^b$ is valid.

Table 1. Porosity metrics and their determination

Porosity metric	symbol	Centrifuging	XRT imaging
Total brine porosity	ϕ	Sum of ϕ_{cen} and ϕ_{res}	Sum of ϕ_{opn} and ϕ_{cls}
Open brine porosity (infinite cluster)	ϕ_{eff}	ϕ_{cen} – centrifuged brine volume fraction	ϕ_{opn} – Imaged air volume fraction (centrifuged brine) open to any sample side
Closed brine porosity	$1 - \phi_{eff}$	ϕ_{res} – residual brine volume fraction based on salinity S_{ir} and temperature T	ϕ_{cls} – Imaged volume fraction of closed brine pores (converted to in situ temperature)
Connected brine porosity (here: vertically)	ϕ_{zz}	not determined	ϕ_{zz} – Imaged air volume fraction (centrifuged brine) open to both vertical sides
Air porosity (closed)	ϕ_a	not determined	ϕ_a – Imaged closed air volume

2.6.1 Porosity and volume fractions

In the present study we shall neglect solid salts and divide the total porosity of sea ice into the volume fractions of brine ϕ and air ϕ_a. The porosity metrics relevant for our study are summarised in Table 1. In general, the brine porosity ϕ is considered as the sum of a connected (infinite cluster) part ϕ_{eff} and a closed (disconnected) part $\phi - \phi_{eff}$. We use both ϕ_{cen} from

190 centrifugation and ϕ_{opn} from the CT image analysis to estimate the open porosity. The closed brine porosity can be obtained either from the salinity of melted centrifuged samples ϕ_{res} or by image analysis ϕ_{cls}. Air porosity ϕ_a is only available through CT image analysis.

The open and closed fractions may be scale dependent. E.g., a closed cluster of brine inclusions could appear open in small samples. Another effect of finite sample sizes is that, because channels are not strictly vertical, some are running out to the

195 sides. The porosity metric relevant for the permeability simulations is thus the volume fraction that connects the upper and lower side of an ice sample, henceforth noted as connected porosity ϕ_{zz}.

For the air porosity we assume that all air is contained in closed air inclusions entrapped in the ice and just define one ϕ_a term. Air bubbles contained in open brine pores are not detected by our approach, as they likely are centrifuged out with the brine.

200 We obtain the porosity metrics ϕ_{opn}, ϕ_a, ϕ_{zz} and ϕ_{cls} with the GeoDict module Porodict, that can be set to determine for any material the porosity open to a specific side (we use all sides) of a CT image. While ϕ_{opn} and ϕ_{zz} are associated with the centrifugation temperature (-2 to -10 °C), the porosity fraction ϕ_{cls} has to obtained from the brine porosity ϕ_{cls16} imaged at the CT operation temperature (-16 °C) by using the equations from Cox and Weeks (1983).

Table 2. Characteristic pore scales

Length scale [a]	symbol	CT image analysis approach
Open brine pore size	D_{opn}	Median of the open air pore size distribution
Closed brine pore size	D_{cls}	Median of the closed brine pore size distribution
Air pore size	D_{air}	Median of the closed air pore size distribution
Brine pore throat size	D_{thr}	Median of open air throat size distribution, determined by virtual porosimetry
SSA length scale	D_{ssa}	Specific surface area (SSA) length scale, obtained from SSA assuming all pores are infinite circular cylinders: $D_{ssa} = 4SSA/\phi$
Maximum path diameter	D_{pth}	Diameter of the path that connects the sample surface and bottom (vertical direction)
Maximum path length	L_{pth}	Length of the path that connects the sample surface and bottom (vertical direction)

[a] All median values are volume-based

2.6.2 Pore size characteristics

205 We define characteristic pore scales in correspondence to the different porosity metrics, given in table 2. For the pore space analysis we also used the GeoDict module Porodict. It offers two algorithms to obtain a pore size distribution (GeoDict, 2012-2020).

The first uses a sphere fitting algorithm to determine the fraction of the pore space that belongs to a certain diameter interval. The algorithm thus determines the minor axis of a cylinder with elliptical cross section. This is done for open and closed air

210 and brine pore classes. From the distribution we obtain the median, in terms of volume. The results from this analysis are the *open brine pore size* D_{opn}, the *closed brine pore size* D_{cls} and the *air pore size* D_{air}.

The second algorithm is based on the virtual injection of spheres into the sample to determine the fraction of the pore space that can be accessed through a sphere of a given radius. The latter is a *porosimetry* (**?**).g., []Dullien1991 algorithm that determines an effective volume distribution of pores limited by throats, and is termed *throat size* in the following. We obtain

215 the *median throat size* D_{thr} as a global measure, by injection of spheres from all 6 directions neck or throat sizes in the pore network.

We obtain two further characteristic length scales. One is the maximum path diameter D_{pth}, which is the maximum diameter of a sphere that can pass through the sample. This lengthscale is of interest for the permeability, and it is easy to determine. The second lengthscale is based on the specific surface area (SSA) of the samples (here defined as internal surface per sample
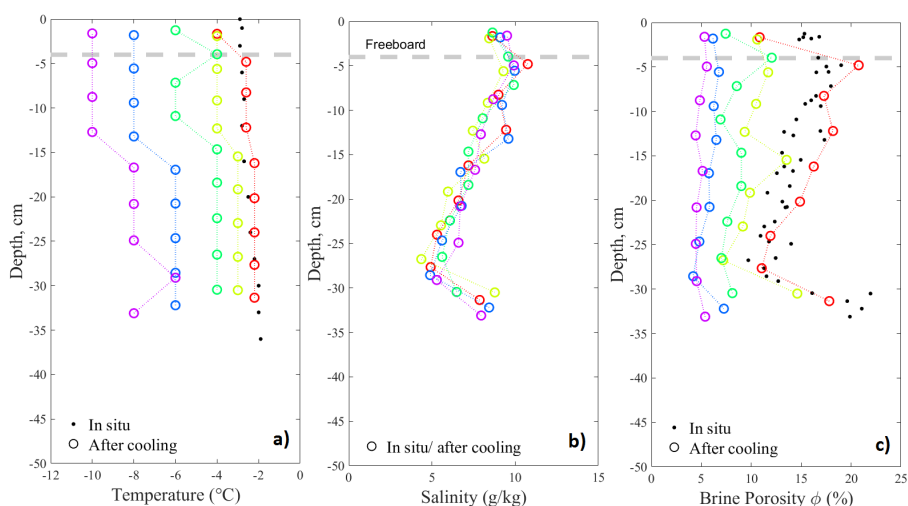
Figure 3. Properties of 5 + 1 sea ice cores obtained on 16.03.2011 in Adventbay, Svalbard. a) In situ ice temperature shown as black dots, 5 lowered centrifugation temperatures as coloured circles. b) Bulk salinity obtained from centrifuged brine and melted residual ice in colors. c) Brine porosity ϕ based on thermodynamic equilibrium shown. Black dots show in situ values, while coloured circles give the brine porosity for the lowered centrifugation temperatures.

220 volume), also determined in PoroDict. If all pores are uniform and parallel cylinders, then their diameter may be related to SSA through $4\phi/SSA$, which shall be defined here as length scale D_{ssa}.

3 Results

3.1 Temperature and salinity

The ice thickness (35 cm on average) did not change measurably during our sampling period, the thickness range was 33 to 36

225 cm for the 18 cores obtained. Here we focus mostly on the cores obtained on 16.04. - all cores from this date were CT-scanned and analysed using the methods described above. The ice had a surface (ice-snow interface) temperature of -2.9 °C and a near bottom interface near the freezing point of seawater (-1.9 °C). Figure 3a shows the *in situ* temperature profile as well as the temperatures to which the 5 microstructure cores were lowered prior to centrifugation. Figure 3b and c show the corresponding salinity profiles and brine volume profiles. For the brine volume also the *in situ* values are given as black dots.

230 The salinity of the ice was obtained from mass and salt balance of the centrifuged brine and the cut residual ice samples. We also obtained salinity profiles for the earlier (14.03.) and later (19.03.)sampling dates (and did the same cooling and centrifuging experiments). As for the ice thickness the salinity did not change measurably during this period. The salinity profile shows the well known C-shape, with some indication of drainage at the very surface above the freeboard [2]. All 5 salinity profiles are

---

[2]Note that, what is indicated as 'freeboard' in the figure, refers to the ice without the freshly fallen snow
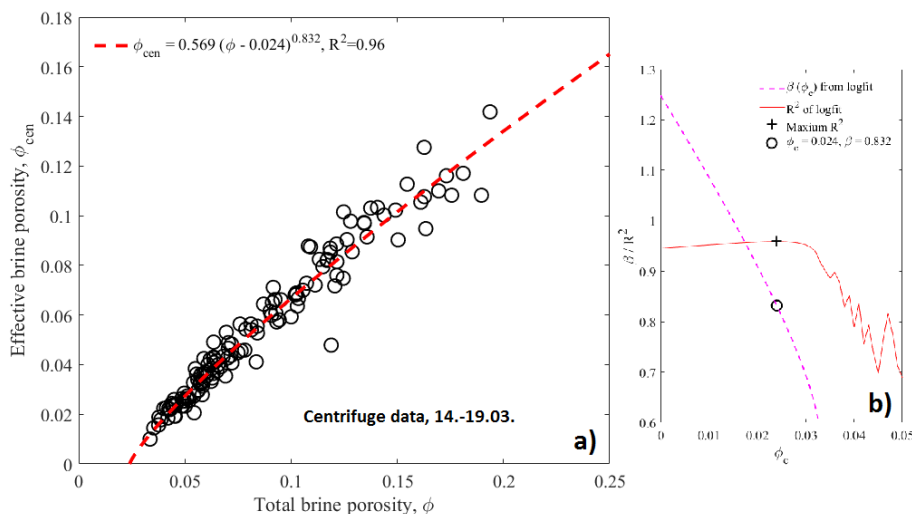
Figure 4. a) Relationship between centrifuged brine porosity ϕ_{cen} and total brine porosity ϕ, based on 15 young ice cores of 35 cm length. b) Optimum exponent $beta$ versus ϕ_c and the corresponding R^2 of double-logarithmic least square fits.

very similar and show little variability. This gives confidence that the temperature dependence during our cooling sequence, not internal variability of the cores, will dominate the results.

3.2 Porosity

3.2.1 Centrifuged porosity

In Figure 4a the centrifuged brine porosity ϕ_{cen} obtained in the centrifuge experiment is shown in dependence on the total brine porosity ϕ. This plot is based on all 15 ice cores from the 3 sampling dates, and thus 145 subsamples of 3-4 cm thickness. The data indicate that at a certain total porosity ϕ_c the ϕ_{cen} becomes zero. To find this threshold we have regressed ϕ_{cen} against $(\phi - \phi_c)^\beta$ to obtain the optimum pair of ϕ_c and the critical exponent β. The result is the equation

$$\phi_{cen} = 0.569(\phi - 0.024)^{0.832} \qquad (6)$$

and shown in Figure 4a as a red dashsed curve. Figure 4b shows the regression results in terms of the dependence of β on ϕ_c. The red curve shows the maximum R^2 corresponding to this $\beta(\phi_c)$ curve. The maximum $R^2 = 0.96$ is found at $\phi_c = 0.0240$. For the exponent $\beta = 0.832$ the 95% confidence bounds from the logfit are [0.803, 0.861]. For the critical ϕ_c we obtain confidence bounds of [0.23,0.27]. Note that a linear fit with $\beta = 1$ would give $\phi_c = 0.011$, as we calculated earlier (Maus et al., 2013). The present analysis shows that the critical exponent β differs significantly from one.
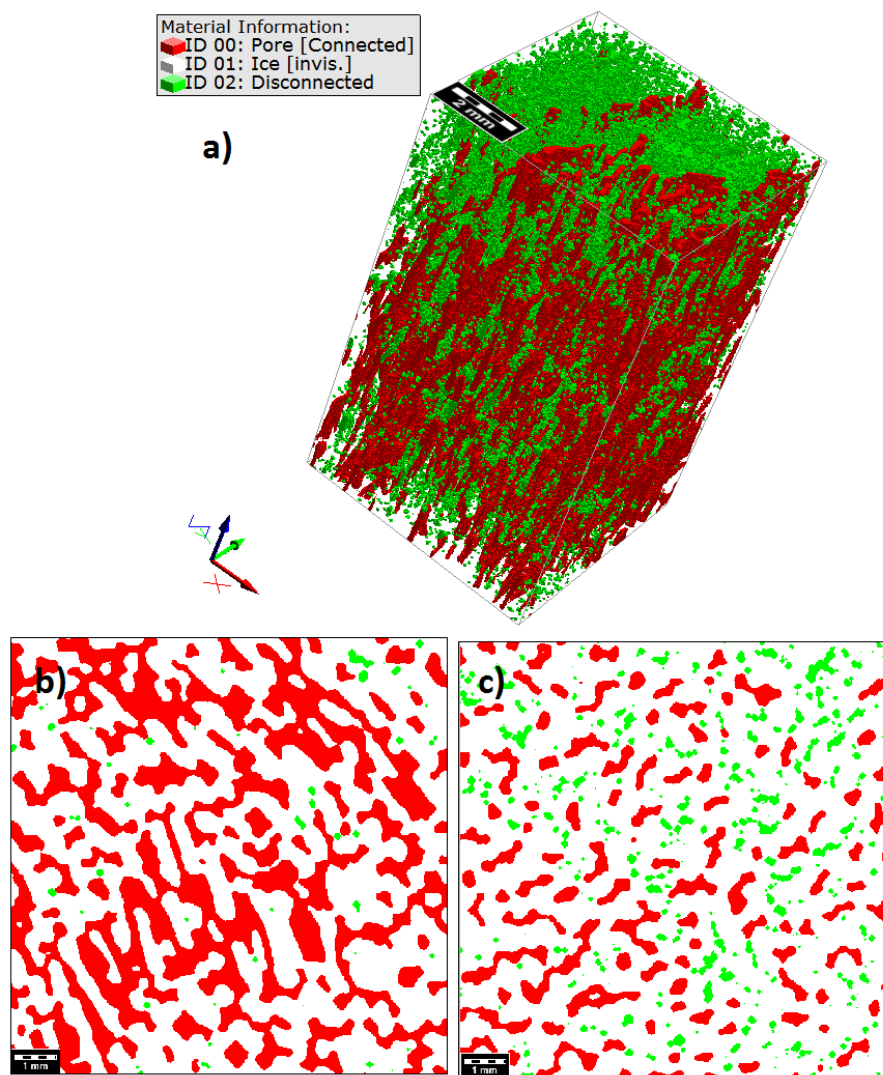
Figure 5. XRT microtomographic images illustrating the open (red) pores and closed (green) brine pores in young sea ice. a) 3D image, ice being invisible; b) horizontal section from the 3D image with open pores dominating, ice being white; c) horizontal section from the 3D image with a similar fraction of open and closed pores. The 2D scale bar is 1 mm, the side length 10.8 mm.

3.2.2 CT-based open porosity

The CT imagery allows us to view the morphology of closed and open pores in some detail, which is illustrated in Figure 5a to c. For better visibility 5a is cropped from the center of the original image (to 1/2 horizontally). Ice is made invisible to illustrate the disconnected (in green) and connected pores (in red). Connected is here used synonymously to open, that is the pore is open to any of the 6 lateral boundaries of the 3-d image.
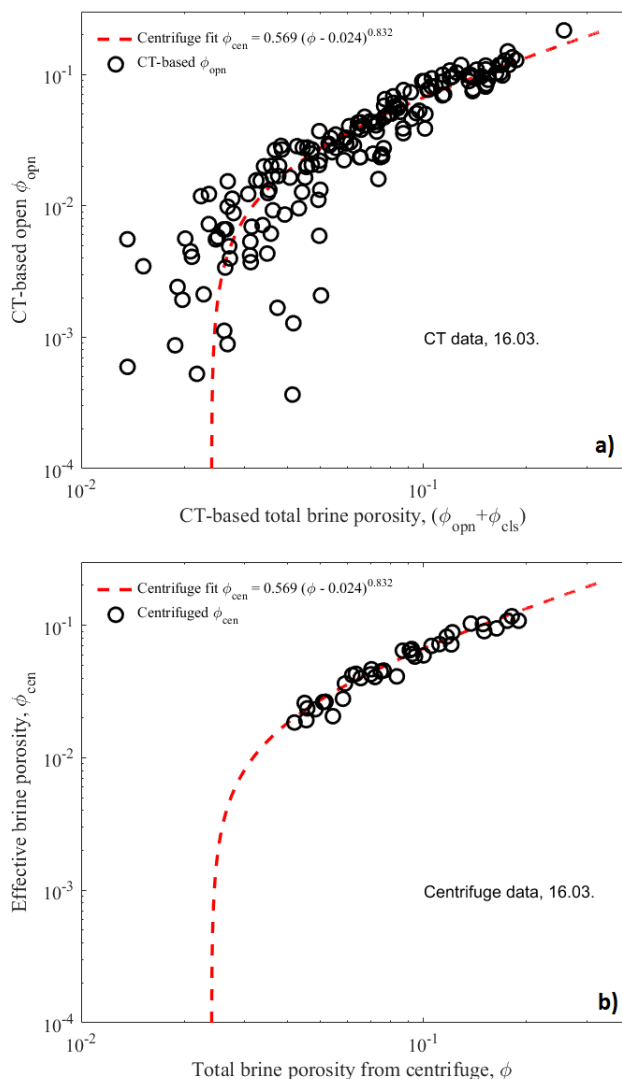
Figure 6. a) Relationship between CT-based open brine porosity ϕ_{opn} and CT-based total brine porosity $(\phi_{opn} + \phi_{cls})$, shown as circles, in comparison to the centrifuge based effective porosity fit (dashed red curves. b) the relationship between ϕ_{cen} an ϕ for the same ice core samples (a 5 core subset of the 15 ice cores in Figure 4a

The horizontal slices are taken from two different regimes of this image, one with predominately connected (5b) and one with a similar fraction of connected and disconnected pores (5c). In the predominately connected Figure 5b one observes a high degree in horizontal connectivity. The patterns appear well resolved by the present voxel size (of 18μm). One also can see that there are many bottlenecks (or throats) in the horizontal connectivity, and one can identify some green spots, where inclusion shave pinched off. In Figure 5c with many more disconnected inclusions, the overall connected pore width is smaller and the horizontal connectivity is low. Note however, that the red pores are still connected to one of the sides of Figure 5a.

In Figure 6a we have plotted the CT-based open brine porosity ϕ_{opn} against the CT-based total brine porosity $(\phi_{opn} + \phi_{cls})$
260 for all samples, and compare them to the centrifuge relationship between ϕ_{cen} and ϕ. Figure 6b shows the corresponding centrifuge data for the same 5 ice cores and sampling day, also on a double logarithmic scale (note that Figure 4 and the optimal fit was based on all 15 ice cores from the three sampling dates). It is obvious that the smaller CT samples extend the range from the centrifuge data to lower ϕ and ϕ_{opn} compared to ϕ_{cen}.

Above a total porosity of $\phi \approx 0.05$ the CT-based open porosity agrees well with the $\phi_{eff}(\phi)$ relationship obtained by
265 centrifugation. At lower porosities the CT data still follow the relationship reasonably, in support of the deduced threshold $\phi_c = 0.024$, yet become more scattered. Note that each CT data point represents for a 2 x 2 x 0.55 cm^3 sub-sample, roughly 1/50 of the volume of the centrifuged samples. The scatter may thus be related to centimetre scale internal variability. On the other hand, the scatter may be due to segmentation errors for both ϕ_{opn} and ϕ_{cls} that at low porosities may reach hundred percent.

270 ### 3.2.3 Centrifuge-based open porosity conversion

The CT image based permeability and pore sizes to be presented in the following paragraphs could be correlated to different porosity metrics - the centrifuge effective porosity ϕ_{cen}, the centrifuge-based total porosity ϕ, the CT-based effective and open ϕ_{opn} and the CT-based total brine porosity $(\phi_{opn} + \phi_{cls})$. To make a comparison to other studies, and a general application feasible, the total brine porosity is chosen. However, permeability will depend on the CT-based open porosity ϕ_{opn} or more
275 accurately the connected porosity ϕ_{zz}. The CT porosities in Figure 6a are scattered, and we cannot say to what degree this is due to segmentation errors, small undetected small brine inclusions, and/or redistribution during cooling of the centrifuged sample, in particular for ϕ_{cls}. We thus make the following approach. We use the open porosity ϕ_{opn} in connection with the centrifuge best fitted equation 6, to obtain a CT-based total brine porosity. Hence, all data in Figure 6a are mapped onto the red dashed curve. In this way we preserve the essential property information to which the permeability relates, the open porosity
280 ϕ_{opn}, but present all data in terms of a total brine porosity ϕ that is computed from ϕ_{opn}.

3.3 Permeability

The results of the permeability simulations for all sub samples are shown in Figure 7 in relation to the total brine porosity ϕ (converted from ϕ_{opn}). As noted, this conversion incorporates the percolation threshold $\phi_c = 0.024$ deduced from the centrifugation, into the analysis. The simulations span a permeability range from 8×10^{-15} to 7×10^{-9} m^2. The porosity regime 0.024
285 to 0.33 above the percolation threshold is shown with grey shading. In this regime we found also impermeable samples.

We obtain two relationships between permeability K and total brine porosity ϕ by double-logarithmic least square fitting. Due to the extreme values we use the robustfit.m Matlab function that gives less weight to outliers. Also, only the data with $\phi > 0.031$ was fitted, that is the regime where no impermeable samples are found. The first relation is a simple power law as most frequently used in sea ice studies involving the permeability:

290 $$K = 1.7 \times 10^{-7} \phi^{4.0} \ \ m^2 \tag{7}$$
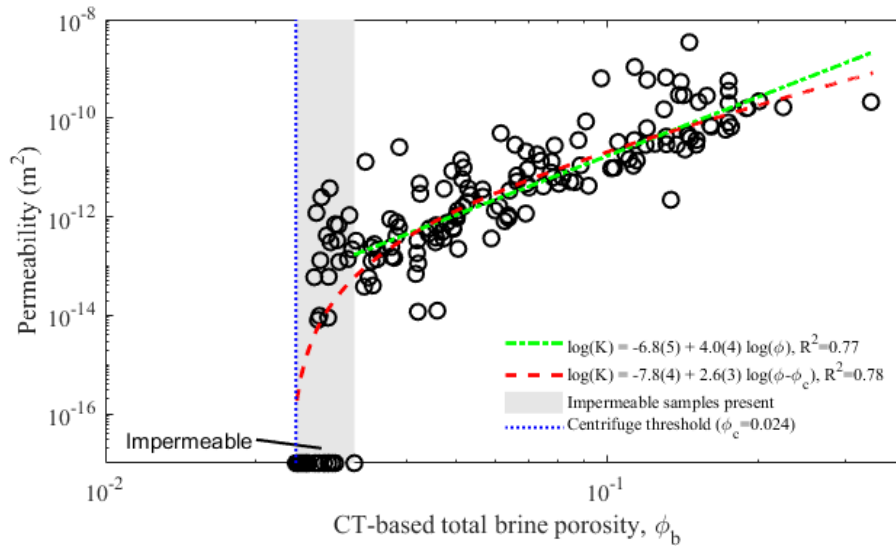
Figure 7. Relationship of simulated vertical permeability K and the total brine porosity ϕ. Two log-log fits are drawn and specified in the legend, one for $K(\phi)$ shown as green curve, one for $K(\phi - \phi_c)$ as red curve. The grey shading indicates the regime where permeable and impermeable samples are found. The numbers in brackets are the uncertainties in the last decimal of the log-log least square fit.

The 95 % significance bounds are a factor of $10^{0.5}$ for the prefactor and 0.4 for the exponent (Figure 7). The second is a percolation-based relationship between between K and $(\phi - \phi_c)$

$$K = 1.7 \times 10^{-8}(\phi - 0.024)^{2.6} \ m^2 \tag{8}$$

Also here, only the data with $\phi > 0.031$ was fitted, trough the relationship is shown for the whole regime to illustrate the
295 percolation behaviour. The 95 % significance bounds are here a factor of $10^{0.4}$ for the prefactor and 0.3 for the exponent. The R^2 of both fits is almost the same. However, Equation 7 does not account for the transition to impermeable samples at low porosities.

At a given porosity the permeability can typically vary over O(2). There are, however, a couple of data points with larger deviation. Figure 8 illustrates the different microstructures to which this behaviour is related. Three examples of sample types
300 have been selected: Type (I) is the most frequent sample type of young ice, with many parallel vertically oriented layers of pores and inclusions. The vertically connected pores are distributed over the whole sample (with total $\phi \approx 10\%$). The computed permeability ($K = 1.0 \times 10^{-11} m^2$) is close to the least squares fits. Type (II) is a sample type, with a rather localised concentration of vertically connected parallel layers and pores. The example has a total brine porosity $\phi \approx 3.3\%$) slightly above the percolation threshold, and the computed permeability ($K = 1.4 \times 10^{-11} m^2$) is 2 orders of magnitude above the
305 fitted relations. Type (III) is a sample type with very low brine fraction of connected pores ($\phi_{zz} \approx 0.06\%$). The example has a total brine porosity $\phi \approx 3.4\%$ slightly above the percolation threshold, and the computed permeability ($K = 4.2 \times 10^{-14} m^2$) closely follows the least squares fit.
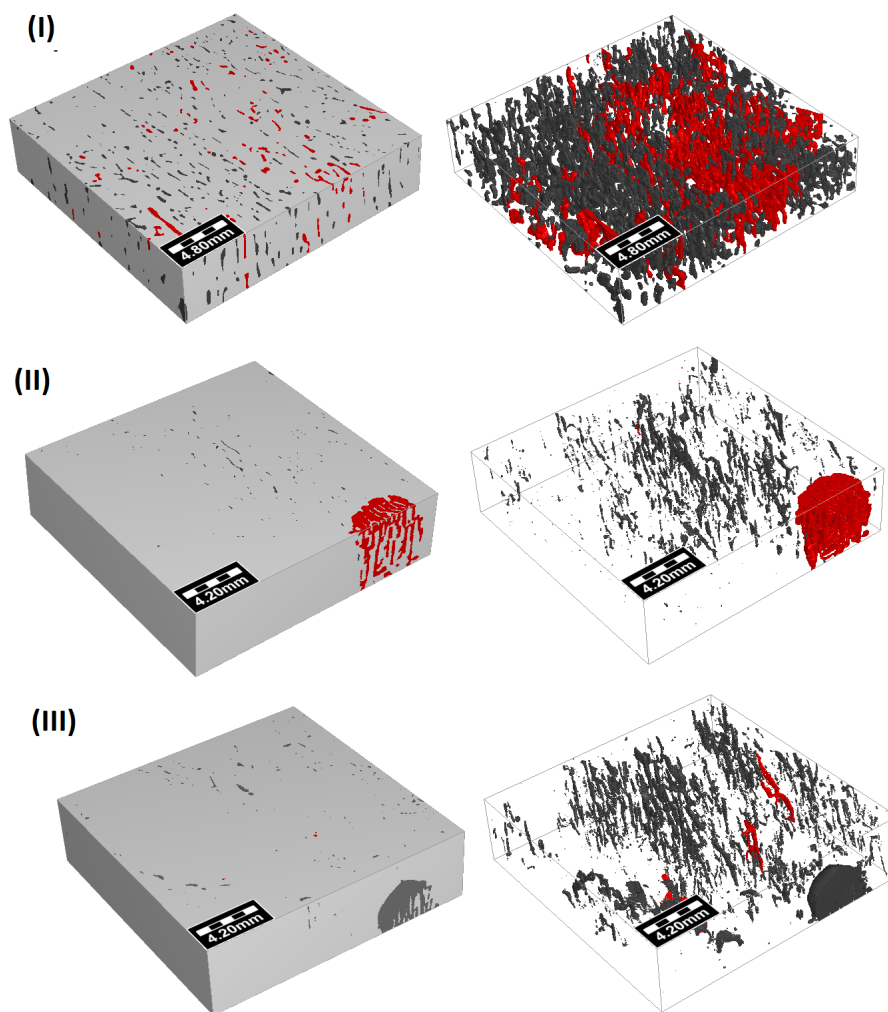
Figure 8. 3D images of typical samples as discussed in the text. The left images are 3D images emphasizing the pores visible at lateral boundaries, the corresponding right images show the pore space with ice being invisible, focusing on the sample interior. Vertically connected pores, contributing to the permeability, are shown i red, other pores in dark grey, ice in light grey. I) Only small pores, half of which are connected; II) One connected large pore, no small ones; III) a few connected small pores and one unconnected large pore running out laterally.

3.3.1 Connected porosity and tortuosity

According to equation 5 the permeability simulations are related to two additional properties. The first is the connected porosity ϕ_{zz}, the second the tortuosity τ of the flow across the sample. For finite size images these may be related in the following way: If the tortuosity approaches or becomes larger than the sample size, then ϕ_{zz} will decrease, because channels will hit the lateral boundaries. Both properties are therefore investigated in Figure 9a and b.
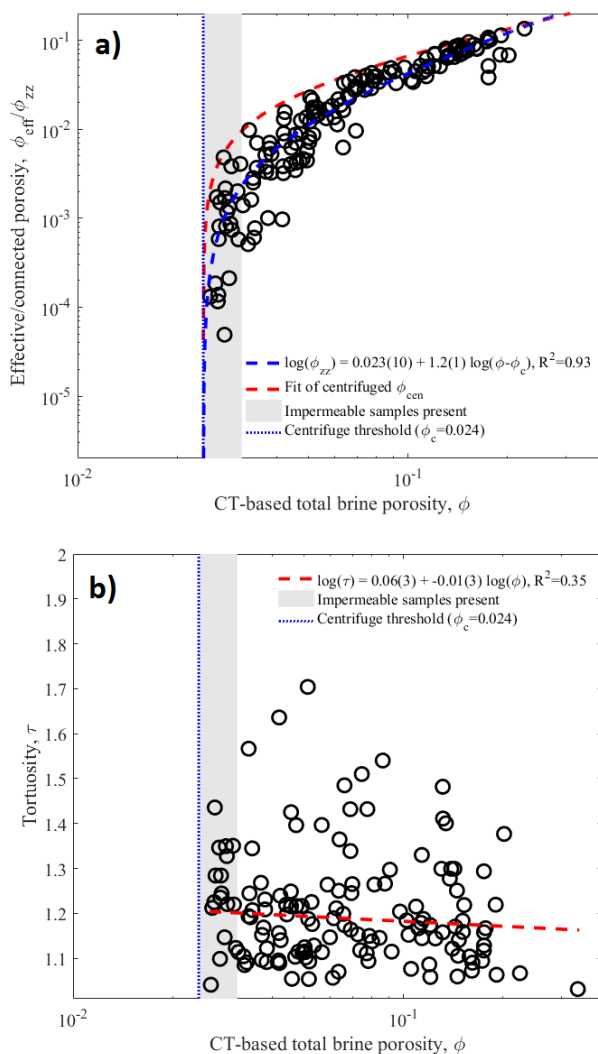
Figure 9. a) Relationship between CT-based connected porosity ϕ_{zz} and total brine porosity, in comparison to the centrifuge based fit of the open porosity ϕ_{cen}. b) Tortuosity of the flow based on the length of the path of the channel with maximum diameter.

Also for the connected porosity in Figure 9a we obtain a double-logarithmic fit of the form $\phi_{zz} \sim (\phi - \phi_c)^b$ and find an exponent $b = 1.2 \pm 0.1$ that is larger than the exponent 0.83 ± 0.03. Comparing the fits in the figure shows that ϕ_{zz} is consistently

315 bounded from above by ϕ_{cen}.

The tortuosity shown in Figure 9b is simply the ratio of the length of the maximum diameter path L_{pth} and the sample thickness L. For this property no measurable change with porosity is observed, indicating that its influence on the permeability can be considered as small.
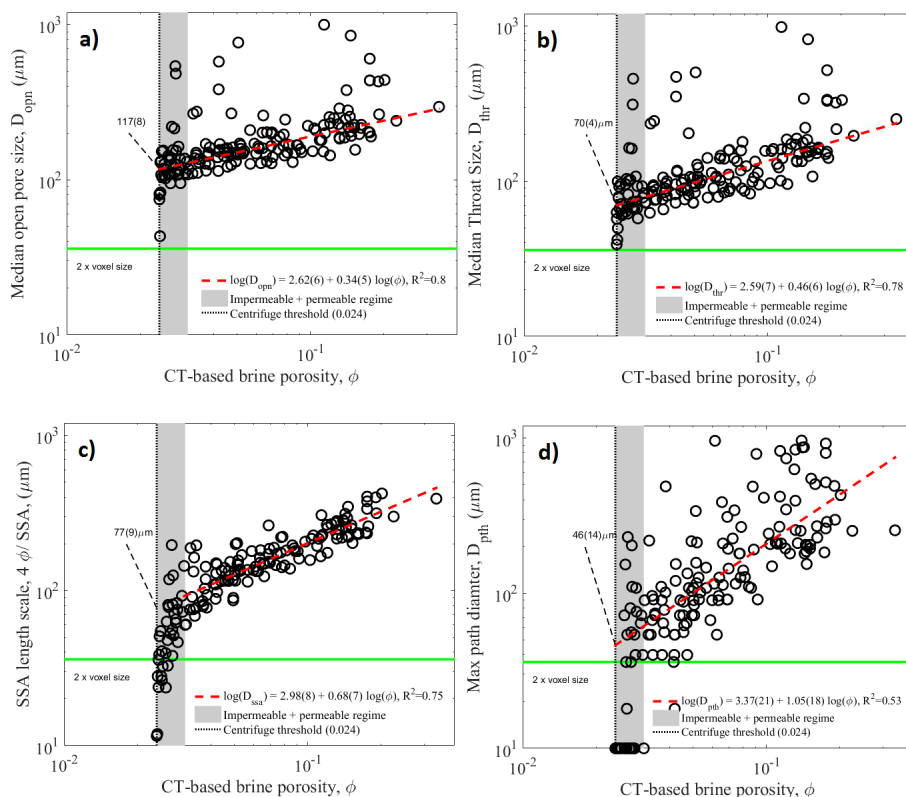
Figure 10. Characteristic pore scales and their dependence on brine porosity. a) Median open pore size D_{opn}; b) Median throat size D_{thr}; c) Pore scale based on specific surface area D_{ssa}; d) maximum path diameter D_{pth}. For all length scales a power law $D \sim \phi^d$ has been determined by double logarithmic least square fit, shown as red dashed line. For D_{ssa} the fit is only based on data with $\phi > 0.031$, outside the regime where impermeable samples are found. The critical pore scales are obtained where the red dashed lines cut the percolation threshold $\phi_c = 0.024$. The Nyquist criterion (2 x voxel size) is shown as a green horizontal line.

3.4 Characteristic pore scales

320 Due to variability also in pore scales, the pore size characteristic scales have been determined as median rather than mean values of the volumetric pore size distribution. Figure 10a to d shows their dependence on brine porosity, and that all pore sizes are increasing with ϕ. This increase has been evaluated by a robust double-logarithmic least squares fit. in order to obtain the power law behaviour of the form $D \sim \phi^e$. This relationship is indicated in the figures. Also shown is the transition regime for which both permeable and impermeable samples have been observed, with grey shading, and a number indicates which scale

325 the fitted power law has reached at the percolation limit of $\phi_c = 0.024$. A green horizontal line marks the length scale of two voxels (36 μm) that often is considered as the Nyquist criterion of digital imaging, which states that the sampling interval has to be at least twice the highest spatial frequency to accurately preserve the spatial resolution. This is of particular importance

Table 3. Pore scale exponents and thresholds

Pore scale D	exponent e in $D \sim \phi^e$	R^2	D at ϕ_c
D_{opn}	0.34 ± 0.05	0.80	$117 \pm 8 \mu m$
D_{thr}	0.46 ± 0.06	0.78	$70 \pm 4 \mu m$
D_{ssa}	0.68 ± 0.07	0.75	$77 \pm 9 \mu m$
D_{opn}	1.05 ± 0.18	0.53	$46 \pm 14 \mu m$

in our study for identification of channels with a path through the sample. A path of just 1 voxel width would very likely be terminated at some level.

330   The results for the open pore size D_{opn} are shown in Figure 10a. Despite a few outliers, weighted less in the robust fit applied, there is a well-defined relationship with a linear slope in log-log space and $D_{opn} \sim \phi^{0.34}$, with $R^2 = 0.80$. Near the percolation threshold a few lower values are seen to drop below the fit.

     The results for the throat size D_{thr} are shown in Figure 10b. They follow in principal the behaviour of the open pore size D_{opn}, yet being typically 1.2-1.7 times smaller, and with a slightly steeper slope $D_{thr} \sim \phi^{0.46}$. Also the throat size shows a

335 drop of a few samples close to the percolation threshold.

     The specific surface area based length scale D_{ssa} is shown in Figure 10c. Here, a linear fit in log-log space obviously does not work for porosities smaller than 0.03, and the grey shaded transition regime has thus been excluded from the fit. The transition of D_{ssa} to lower values then the least square fit (related to larger specific surface) starts at higher porosity than for D_{opn} and D_{thr}. That values drop below the proposed resolution limit is related to an algorithm in GeoDict employing estimates

340 of specific surface more complex than a simple sphere-fitting approach.

     The last length scale to be considered is the maximum path diameter D_{pth}, corresponding to the maximum diameter of a sphere that can permeate through the sample. D_{pth} thus is based on a comparable approach as the throat size D_{thr}. The values are much more scattered than D_{thr}, and their relationship with ϕ has a larger slope with $D_{pth} \sim \phi^{1.05}$, though with less confidence than for the other length scales. It is seen that the lowest values of D_{pth} are close to the resolution limit line below

345 a porosity of $\phi < 0.05$.

     The exponents of the pore scale versus brine porosity relationships as well as the pore sizes at the threshold porosity $\phi_c = 0.024$ are summarised in Table 3.

4   Discussion

We have obtained results for the permeability and pore scales of sea ice through a challenging procedure with the following

350 steps. (i) Field sampling of a large number of cores (15) of uniform ice, (ii) thorough temperature control of samples at in situ values, (iii) centrifuging samples at in situ temperatures, (iv) X-ray microtomographic imaging, (v) pores size analysis and numerical permeability simulations. Also, by lowering the temperatures of harvested ice cores in the lab, we extended the

original *in situ* temperature regime of the samples (minimum -3°C) down to -10°C) and obtained results for brine porosities down $\phi \approx 0.03$.

355   It needs to be pointed out that the centrifugation approach has been essential to obtain the XRT results. XRT imaging, the method of choice for non-invasive imaging of the internal structure of materials (Kinney and Nichols, 1992; Buffiere et al., 2010), is these days increasingly used in the geosciences (Cnudde and Boone, 2013). It has become an important method in snow research (Flin et al., 2004; Schneebeli and Sokratov, 2004; Heggli et al., 2011) and recent work has indicated its potential for sea ice microstructure analysis (Golden et al., 2007; Pringle et al., 2009; Obbard et al., 2009; Maus et al., 2015; Crabeck

360   et al., 2016; Lieb-Lappen et al., 2017). However a limitation for application to sea ice stems from the small X-ray absorption contrast between ice and (sea)water (Bartels-Rausch et al., 2014). Imaging sea ice at lower temperature than in the field gives, due to the corresponding higher salinity of brine, reasonable contrast (Obbard et al., 2009; Lieb-Lappen et al., 2017), yet pore sizes and connectivity will differ from in situ conditions (as clearly shown in the results presented here). XRT imaging has thus been performed on ice grown from salt-water with CsCl added as contrast agent (Golden et al., 2007; Pringle et al., 2009). Such

365   "doping" is not feasible in the field. In the present work, to solve the contrast problem and obtain good images of relatively warm sea ice, the ice samples were thus centrifuged prior to imaging, replacing brine by air with much higher contrast to ice (Weissenberger et al., 1992; Maus et al., 2011, 2015).

4.1   Effective versus total porosity

Centrifuging is not only a means of obtaining high quality XRT microstructure images. It provides the dependence of cen-
370   trifuged (effective) porosity on total brine porosity, as well as a porosity threshold of $\phi_c = 2.4 \pm 0.3\%$. This threshold is a new result compared to most earlier work that has more or less accepted a value of 5%, which will be further analysed below. The derived empirical relationship between effective and total brine porosity, Equation 6, should be relevant for model applications that need to know the effective porosity. The deduced critical exponent 0.83 ± 0.03 is of relevance for model approaches based on percolation theory. In terms of the latter ϕ_{cen} can be interpreted as the probability to belong to the infinite connected clus-
375   ter. So far sea ice permeability has been studied in terms of *isotropic percolation* (Petrich et al., 2006; Golden et al., 2007; Pringle et al., 2009), for which the critical exponent for the infinite cluster strength is known to be $\beta \approx 0.41$ in 3D (Stauffer and Aharony, 1992; Sahimi, 1993). However, in sea ice the growth, pore structure evolution and desalination processes are anisotropic and directed towards the ocean. For such a setting, typical for many natural porous media, already Broadbent and Hammersley (1957) have suggested that the percolation should be directed. *Directed percolation* belongs to a different univer-
380   sality class with critical exponents differing from the isotropic case, $\beta \approx 0.82$ being the presently accepted value for β in 3(+1, the direction) dimensions (Henkel et al., 2008; Hinrichsen, 2009). Our deduced $\beta \approx 0.83 \pm 0.03$ is in close agreement with the latter. On the one hand this gives us strong confidence for the validity of the centrifugation approach and its results. On the other hand it points to the need to analyse sea ice in terms of *directed* rather than *isotropic* percolation.

4.2 Effective versus connected porosity

385 The comparison of CT-based connected porosity ϕ_{zz} and open porosity ϕ_{opn} to in Figure 9a indicates an increasing difference the lower the total brine porosity ϕ. The exponent in $\phi_{zz} \sim (\phi - \phi_c)^b$ is $b = 1.2 \pm 0.1$ compared to the exponent 0.83 ± 0.03 for the open/centrifuged porosity.

We can obtain a simple estimate of the fraction of brine channels that can be expected to open to the sides and not contributing to ϕ_{zz}. Assuming a simple 2D geometry and the all pores are parallel, this fraction will be approximately $tan(\alpha)\epsilon$, where α is 390 the inclination angle of crystals/channels against the vertical and ϵ the ratio of sample height to diameter. For sea ice a typical $\alpha \approx 10°$ has been documented (Kovacs and Morey, 1978; Langhorne and Robinson, 1986; Kawamura, 1988). Freitag (1999) has performed a sensitivity test and found a permeability reduction with sample height that was consistent with $\alpha \approx 10°$. For our $\epsilon \approx 1/4$, the effect is an underestimate by less than 5 %. In the standard experiments from Freitag (1999), with $\epsilon \approx 2/3$, one would expect a slightly larger underestimate of 12 %.

395 From this consideration we conclude that the inclination of crystals alone cannot explain the increasing difference between ϕ_{zz} and open porosity ϕ_{opn}. There must be operating a pore splitting mechanism that disconnects vertical pores that still are connected to the lateral sides, contributing to ϕ_{opn} and not ϕ_{zz}.

4.3 Pore size threshold

In Figure 10a to d we have shown that all characteristic length scales decrease with decreasing porosity. For two length scales, 400 the median open pore size D_{opn} and the median throat size D_{thr}, very robust power law relationships of type $D \sim \phi^d$ were obtained. These relationships do not show percolation behaviour of the form $D \sim (\phi - \phi_c)^e$, but they are supposed to create the percolation behaviour in ϕ_{zz} and ϕ_{opn} as follows. By evaluating the power law relationships at the present percolation threshold ϕ_c, we obtain their critical values at the percolation threshold. Of particular interest is the critical throat diameter

$$D_{thr,c} = 70 \pm 4 \ \mu m, \ \ at \ \phi_c = 0.024 \tag{9}$$

405 at the threshold. We interpret it as the throat diameter at which necking occurs to lock the brine pores.

This result is consistent with two earlier studies of sea ice microstructure. Anderson and Weeks (1958) discussed the transition from brine layers into cylindrical brine tubes in connection with changes in the relationship between sea ice strength and brine porosity. They proposed, based on an analysis of horizontal thin sections, a splitting of layers into channels near a tube diameter of 0.07 mm. These authors have not presented a statistical analysis of their results, but mention that they obtained the 410 value from 'photographs of layers just before and after the splitting'. From the plate spacing reported for their study ($0.46mm$ on average) it may be suspected that they analysed mostly young ice of similar age than ours. The agreement of ours and their result is very interesting. Also Light et al. (2003) studied the temperature dependence of sea ice microstructure, in order to formulate a model for the radiative properties of sea ice. Based on the optical analysis of many samples they distinguished morphologically between brine tubes (above a length of 0.5 mm) and brine pockets (below this value), and derived an equation 415 for the aspect ratio (length L / diameter D) of tubes and pockets ($10.3D = L^{0.33}$). Inserting the pocket-tube transition of 0.5

mm for L one obtains a tube diameter of 0.077 mm at the transition, indicating also here a similar scale for the splitting of tubes.

The critical median open pore size $D_{opn,c}$ computed at the threshold was 117μm, a factor of 1.7 larger than $D_{thr,c}$. This is likely the value that one would identify by considering all pores in a 2D thin section, because one would not know which are

420 the throats. Also noteworthy, though not investigating the temperature dependence or transition from pockets to tubes, is the study by Cole and Shapiro (1998) of Arctic first-year ice at the start, mid and end of the freezing season. These authors were not simply doing 2D thin sections, but sectioned sea ice vertically and horizontally, to obtain the dimensions of brine filaments in three directions (their Figure 9). They found the average width of brine inclusions, at a depth of 0.2 m, to increase from 0.08 ± 0.03 mm to 0.14 ± 0.04 mm (their Figure 10b). The imaging temperature was -14 °Cwhich, with the reported salinities

425 of 5-7 psu, indicates a porosity of 0.022 to 0.031. This condition is similar to the percolation limit in our study, which is supported by the fact that Cole and Shapiro (1998) indeed mostly observed vertically disconnected brine filaments. The range of observed brine inclusion width is consistent with our median open pore size $D_{opn,c}$.

The analysis of pore and throat diameters thus gives us important information about the critical length scales at the percolation transition. More supporting information comes from the specific surface area length scale that we compute by assuming

430 that the surface area relates to infinite pores with circular cross section, which means $D_{SSA} = 4\phi/SSA$. This is the only length scale that appears to show critical behaviour near the percolation threshold. This behaviour indeed supports the necking hypothesis as follows: Consider a long brine pore that splits into spherical inclusions. While D_{opn} and D_{thr} will not change much, the SSA does increase during the transition to spheres. However, to account for this in the length scale computation one would have to calculate $D_{SSA} = 6\phi/SSA$. As this is not done for the data points in Figure 10c, there is an apparent drop in

435 our computed D_{ssa} when splitting takes place, nicely seen in our data.

But we can, through D_{ssa}, not only identify the necking and splitting near the percolation threshold. When considering the power law fits $D \sim \phi^d$ one would expect that, if decreasing D_{SSA} with ϕ would only relate to diameter changes, it should be described by a similar exponent d as D_{opn} (0.34 ± 0.05) and D_{thr} (0.046 ± 0.06). However, also if the fit is restricted to the regime $\phi > 0.031$ we find an exponent (equivalent to the slope in log-log space) that is larger for D_{ssa} (0.68 ± 0.07). The

440 interpretation is that slitting and necking operates over the whole porosity regime in our dataset.

The critical value of $D_{thr,c} = 70\mu$m should be interpreted as a statistical descriptor of the pore space, rather than a strict limit. Looking at the fourth characteristic length scale, the maximum path diameter D_{pth} in Figure 10d, we see that there exist through-flow paths with lower diameter. This is not unexpected in the sense that the throat size distribution only has its median at 70μm at the transition. For a more detailed discussion the present dataset is somewhat limited here, as the lower range of

445 the identified maximum path diameters touches the Nyquist spatial criterion of 36μm below a porosity of 0.05. Figure 10d indicates that, to study the necking transition near the percolation threshold dynamically, one would likely have to increase the present resolution by at least a factor of two.

Regarding the mechanism of necking, Anderson and Weeks (1958) had once argued that the necking of pores is driven by surface energy effects. However, one of us has argued that (i) the original brine layers are expected to be low energy surfaces

450 and that (ii) latent heat energy fluxes during freezing are many orders of magnitude larger than surface energy transitions
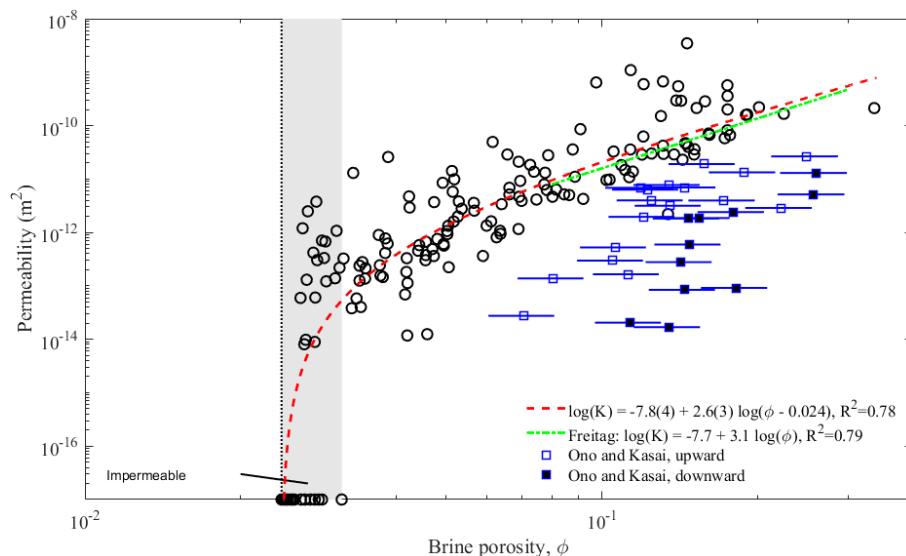
Figure 11. Relationship of simulated vertical permeability K and $(\phi - \phi_c)$ as shown in Figure 7 as red dashed curve, here compared to two earlier investigations from Freitag (1999) and Ono and Kasai (1985). The grey shading indicates the regime where permeable and impermeable samples are found.

(Maus, 2007). Due to these factors it seems more likely that morphological freezing instabilities in supercooled brine layers play a role for the necking. A concise physical explanation for the necking phenomenon is lacking so far.

4.4 Permeability

Having found consistent explanations of the observed percolation limit in terms of critical pores sizes, we now return to the

455 permeability simulations. In Figure 11 we compare our results to the results of two experimental studies on young ice.

The relationship based on the work by Freitag (1999) is likely the most frequently cited and used in the literature. Freitag only documented the data points of K versus the centrifuged brine porosity ϕ_{cen}, yet he has given the relationship between K and total brine porosity ϕ. It is given in the legend of Figure 11 and plotted as a green dashed curve. The porosity range for Freitag's fit ($0.07 < \phi < 0.3$) has been estimated from the ϕ_{cen} values he reported. Comparison with our fit (the red dashed

460 curve) indicates a very good agreement with Freitag's results for his porosity range of validity. The maximum difference is just 30%. As the confidence bounds for our fit indicate roughly a factor of 2, there is no significant difference in the predictions. However, our relationship is based on a fit of observations down to $\phi = 0.03$, and allows to estimate permeabilities at low porosities, where Freitag's relationship is not applicable.

The second dataset is from experiments that Ono and Kasai (1985) performed with artificially grown young ice. These

465 authors did not publish the permeability but the hydraulic conductivity, and we have used Equation 3 to convert from $\overline{V}$ to permeability K. To do so we used the temperature and brine salinity dependent kinematic viscosity relationship from Maus (2007). As Ono and Kasai only reported surface temperatures of their tested ice, we make the assumption that the salinity is

similar to those reported for ice growth experiments from other laboratory studies. For the documented ice growth velocity of 10^{-4} cm/s and water salinity ($S_w \approx 33\,\%o$ NaCl) a 6 cm thick sea ice crust will typically contain 40 to 50% of the salinity of

470 water from which it grows (Wakatsuchi, 1974, 1983). We thus assume a sea ice salinity of $S_i \approx 14 \pm 2\,\%o$ NaCl. We shall use this range with reported surface temperatures to estimate the brine volume ϕ at the surface of the ice. This leads to the blue data points and uncertainty estimates in Figure 11. There are two sets of data. The open squares are based on measurements of upward movement, where Ono and Kasai created a pressure gradient directed from the water into the ice. The filled squares are based on measurements of downward movement, where the authors poured brine, in salinity equilibrium with the surface

475 temperature, onto the ice. The surface temperature was adjusted with an infrared lamp.

It is seen that the permeability data from Ono and Kasai (1985) fall 1-2 orders of magnitude below our and Freitag's observations. The error bounds indicate that this hardly can be explained by a lower salinity of freshly grown ice (at 10^{-4} cm/s) than assumed. We think that the difference is related to two factors. The first is related to the fact that, in contrast to our and Freitag's study of sub sample permeability, Ono and Kasai measured the permeability of the full ice thickness (of however

480 only 6 cm). In this setting the ice surface, where the ice is coldest, will control the permeability. However, in most cases the first surface ice skim is growing much faster, implying smaller crystals (or plate spacing) and thus more tiny pores between them, with strong impact on the permeability (e.g., Okada et al., 1999). In addition to crystal size a more random crystal orientation may imply tortuous flow and decrease the permeability further. The second factor is likely related to changes in the microstructure during the experiments, also discussed by Freitag (1999). Assume that the upward flow experiments were

485 performed first. As during the flow less saline seawater is exchanged against brine, the ice salinity will decrease. At high surface temperatures (similar to those in the seawater) this salinity decrease is low, yet it becomes large with the temperature difference between the ice surface and the water. This is consistent with larger deviations of the data points from Ono and Kasai from our permeability fit at lower brine porosity. If the downward flow experiments were than to take place after the upward flow, salinities could have been considerably less than assumed for freshly grown ice. The argument also works vice versa, to

490 explain the difference in the upward and downward results, as during downward flow of high salinity brine the bulk salinity of an ice sample is expected to increase. Based on these arguments, the large deviations of the data from Ono and Kasai (1985) can be understood at least qualitatively. However, their experimental data are very likely not suited to validate arguments for percolation transitions in sea ice, as once proposed by Golden et al. (1998).

We recall that the double-logarithmic fit in Figure 11 is only based on our data above $\phi = 0.031$, excluding the regime where

495 we find permeable and impermeable samples. The investigation of the characteristic pore scales, in particular the maximum path diameter shown in Figure 10d, also indicates that we start facing resolution problems below a brine porosity of $\phi \approx 0.04$. This, as well as image segmentation errors, may to some degree explain that the data points in the regime $0.024 < \phi < 0.031$ appear significantly above our proposed relationship. And one can argue, that some kind of averaging of zero permeabilities with these high values would move the data closer to the fitted percolation curve. As our data in this regime are not of high

500 enough quality we have not applied such a correction. However, the combination of good enough image quality above $\phi \approx 0.04$ has, in combination with the threshold $\phi_c = 0.024$ from the centrifuge experiments, enabled us to deduce Equation 8 with good confidence, at the same time being consistent with the work from Freitag (1999).

Over the whole range of porosities, we find some samples with O(2) larger permeabilities than the fitted curve and most data points. As discussed above these are associated with type (II) ice samples in Figure 8 and the presence of larger brine

505 channels. Such a dual system of pore sizes is a frequently described, yet but in detail still little explored, feature of sea ice (e.g., Wakatsuchi, 1983; Weeks, 2010; Rees Jones and Grae Worster, 2014). That only part of our samples do contain larger brine channels is likely related to our limited sample size (horizontally 2 cm), in turn leading to the scatter in permeabilities. However, the large number of samples, and the additional constraint $\phi_c = 0.024$ from centrifuging larger samples, has allowed us to obtain a statistically robust relationship between K and ϕ. Yet the uncertainty is still O(100%). Improvements may be

510 made on the basis of currently available X-ray detectors that allow for a 2 times larger field of view (at the same spatial resolution), with a better representation of the dual brine pore size networks.

4.5 Porosity threshold

As already mentioned, the present analysis has led us to deduce a porosity threshold of $\phi_c = 2.4 \pm 0.3\%$, just half of the value of $\phi_c = 5\%$ proposed in most earlier work. The latter hitherto accepted threshold has been based on different assumptions and

515 approaches that we now are able to address.

The apparently most stringent approach to estimate ϕ_c was proposed by Pringle et al. (2009) and also based on the analysis of CT images. These authors focused on the vertical connectivity ϕ_{zz} and investigated its scale dependence to estimate the connectivity threshold based on assumptions from isotropic percolation theory (Stauffer and Aharony, 1992). They investigated artificial sea ice images, cubic and with side lengths 0.2 to 0.7 mm. From the scale dependence of ϕ_{zz} they deduced a critical

520 value of $\phi_c = 4.6 \pm 0.7$ % for the vertical percolation threshold. What is most problematic with this analysis, is likely the voxel size of 41.4μm, for which we suspect a (Nyquist criterion limited) detectability of connected pores 83μm, two times the voxel size. As even in our study (with 36μm for comparison) we are observing larger scatter in connectivity and pore scales, when the porosity threshold is approached, we suppose that such problem likely has influenced the percolation behaviour of the samples from Pringle et al. (2009). And, considering our deduced critical throat size of 70μm, a similar value would not have been

525 resolved by imagery with a 83μm Nyquist criterion. A simplistic quantitative argument may be obtained by looking at Figures 10b for the throat size D_{thr} and 10d for the maximum path diameter D_{thr}. We can ask at which porosity the lowest observed values drop below 83μm, which indeed happens in the range $5 < \phi < 6$ %. Finally, though likely of minor importance, the results from Pringle et al. (2009) can be expected to change if critical exponents for directed rather than isotropic percolation, supported by the present study, would have been used in the derivation.

530 The first proposal of a critical brine porosity $\phi_c = 5\%$ has once been proposed by Cox and Weeks (1988), based on observations of observed salt fluxes from sea ice. The data has been later analysed by Petrich et al. (2006), coming to the same conclusion that sea ice desalination is restricted to brine porosities above $\phi_c = 5\%$, arguing that this is the percolation threshold. There is a problem with this argument: It is not the vertical permeability that has been observed, but the desalination of the ice. The latter however depends on other factors, like the brine salinity gradient in the ice and a certain degree of horizontal

535 permeability to drive internal flow. What can be stated is: the analysed data may be interpreted to represent a porosity threshold at which convection sets in, rather than at which the ice becomes impermeable.

Another proposal of a critical brine porosity $\phi_c = 5\%$ was once published by Golden et al. (1998), and based to some extent on the experiments from Ono and Kasai (1985) discussed above. However, on the one hand, our analysis above indicates that the experiments from Ono and Kasai (1985) were likely far away from a porosity of $\phi \approx 5\%$ and can not validate any behaviour near that porosity. On the other hand, there is reason to believe that the ice salinity has changed during these experiments, making the results difficult to interpret. In any case, comparison to our simulations indicates that the data points from Ono and Kasai (1985) can hardly be associated with a percolation threshold.

Based on these considerations we cannot see support of a percolation threshold of $\phi_c = 5\%$ and think that this value needs to be revised. While the present value of 2.4% applies to young ice that has grown at moderate growth rates (2-5 cm/day for both our and Freitags experiments), we would expect that this threshold is not a constant for sea ice but depends on growth conditions. The basic argument is that, if the critical length scale for necking of throats controls the transition, the critical brine volume ϕ_c may be expected to simply scale inversely with the spacing of these throats. Assuming that this spacing is proportional to the basic brine layer or plate spacing a_0, one would expect that $\phi_c \sim a_0^{-1}$, implying that the percolation threshold in slower growing ice (with larger a_0) should be smaller.

5 Conclusions

We have investigated the percolation behaviour of young Arctic sea ice in terms of the two non-destructive techniques (i) centrifuging of brine for separation of the connected and disconnected pore space and (ii) 3D X-ray microtomographic imaging followed by direct numerical simulations of the permeability and an analysis of the relevant pore size characteristics. Our main findings are

- We obtain a confident relationship between centrifuged (effective) porosity ϕ_{cen} and total porosity ϕ

- The relationship $\phi_{cen}(\phi)$ strongly supports that sea ice should be analysed and modelled in terms of *direction percolation* theory, rather than its *isotropic* variant so far applied to sea ice problems.

- We further find that the relationship $\phi_{cen}(\phi)$ is consistent with a connectivity threshold at a porosity of $\phi_c = 2.4 \pm 0.3\%$. This value is considerably lower than the commonly accepted 5% based on earlier investigations (Golden et al., 1998; Cox and Weeks, 1988; Petrich et al., 2006; Golden et al., 2007; Pringle et al., 2009).

- Our pore scale observations near the percolation threshold indicate that earlier estimates of ϕ_c were likely limited by a too coarse spatial resolution, or cannot be strictly related to a percolation threshold.

- We associated the percolation transition with the necking of brine pores, identified it with the median of the critical pore throat diameter distribution, and obtained an estimate of the critical throat diameter or width $D_{thr,c} \approx 0.07$ mm at the transition. This finding is consistent with pore size analysis from earlier studies.

- We derived a novel consistent parametrisation of vertical permeability K based on total brine porosity ϕ that is valid for the porosity range 0 to 20 %, improving and extending earlier work.

The centrifuge approach requires very good logistics, like the field operation of several temperature control boxes and a refrigerated centrifuge. Yet it has several other advantages related to the challenge to really image the in situ sea ice mi-

570 crostructure. A well known problem for high porosity samples is brine loss during sampling, which in uncentrifuged samples would show up as a lot of air. By centrifuging all connected brine out, this problem is solved and connected and open air deduced by image analysis. Replacing the interconnected brine by air makes not only XRT imaging of the emptied pore networks possible, it also makes microstructure changes during storage and transport much less a problem.

The present work presents new insight into the sea ice pore space evolution and theoretical interpretation of the latter, and

575 demonstrates the large potential of 3D X-ray micro-tomographic imaging to make progress in our fundamental understanding of sea ice properties. Future studies should verify the present results with slightly higher resolution.

Data availability. The data are very large 3D images, in total almost 1 TB in size. It is planned to make the data available in the future within a larger infrastructure project. Currently data will be made available to interested scientists upon contacting the corresponding author.

Author contributions. SM performed the field experiments, the data analysis and writing of the first manuscript. SM performed the X-

580 ray scanning with support from MS and his working group. SM run the permeability simulations and pore space analysis using Geodict with support from AW and Math2Market. All authors contributed to rewriting and submission of the manuscript. All authors improved the manuscript contributed to field data acquisition and contributed to writing of the manuscript.

Competing interests. All authors declare no competing interests.

Acknowledgements. This project was partly funded through the Research Council of Norway (RCN) program PETROMAKS2 grant 243812

585 (Microscale Interaction of Oil with Sea Ice for Detection and Environmental Risk Management in Sustainable Operations, MOSIDEO, 20015-2020) as well a the RCN grant 218407 (Microstructure and phase transitions of sea ice, MIPHASICE, 2011-2012).

References

Anderson, D. L. and Weeks, W. F.: A theoretical study of sea ice strength, Trans. Amer. Geophys. Union, 39, 632–640, 1958.

Bartels-Rausch, T., Jacobi, H.-W., Kahan, T. F., Thomas, J. L., Thomson, E. S., Abbatt, J. P. D., Ammann, M., Blackford, J. R., Bluhm,
H., Boxe, C., Domine, F., Frey, M. M., Gladich, I., Guzmán, M. I., Heger, D., Huthwelker, T., Klán, P., Kuhs, W. F., Kuo, M. H.,
Maus, S., Moussa, S. G., McNeill, V. F., Newberg, J. T., Pettersson, J. B. C., Roeselová, M., and Sodeau, J. R.: A review of air-ice
chemical and physical interactions (AICI): liquids, quasi-liquids, and solids in snow, Atmospheric Chemistry and Physics, 14, 1–47,
https://doi.org/doi:10.5194/acp-14-1-2014, www.atmos-chem-phys.net/14/1/2014/, 2014.

Broadbent, S. R. and Hammersley, J. M.: Percolation processes, Mathematical Proceedings of the Cambridge Philosophical Society, 53,
629–641, https://doi.org/doi:10.1017, 1957.

Buffiere, J., Maire, E., Adrien, J., Masse, J., and Boller, E.: In situ experiments with X-ray tomography: an attractive tool for experimental
mechanics, Exper. Mechan., 50, 289–305, 2010.

Cheng, L., Rief, S., and Wiegmann, A.: Simple FFT for flow computations in low porosity microCT images, urn:nbn:de:0011-n-3641306,
poster presented at Interpore 5th International Conference on Porous Media 2013, Prague, 2013.

Cnudde, V. and Boone, M.: High-resolution X-ray computed tomography in geosciences: a review of the current technology and applications,
Earth-Science Rev., 123, 1–17, 2013.

Cole, D. M. and Shapiro, L. H.: Observations of brine drainage networks and microstructure of first-year sea ice, J. Geophys. Res., 103,
21 739–21 750, 1998.

Cox, G. F. N. and Weeks, W. F.: Equations for determining the gas and brine volumes of sea ice samples during sampling and storage, J.
Glaciol., 32, 371–375, 1983.

Cox, G. F. N. and Weeks, W. F.: Numerical simulations of the profile properties of undeformed first-year ice during the growth season, J.
Geophys. Res., 93, 12 449–12 460, 1988.

Crabeck, O., Galley, R., Delille, B., Else, B., Geilfus, N., Lemes, M., Roches, M., Francus, P., Tison, J., and Rysgaard, S.: Imaging air
volume fraction in sea ice using non-destructive X-ray tomography, The Cryosphere, 10, 1125–1145, https://doi.org/10.5194/tc-10-1125-
2016, 2016.

Dullien, F. A. L.: Porous Media: Fluid Transport and Pore Structure, Academic Press, 2nd edn., 574 pp., 1991.

Flin, F., Brzoska, J. B., Lesaffre, B., Coleou, C., and Pieritz, R. A.: Three-dimensional geometric measurements of snow microstructural
evolution under isothermal conditions, Annals Glaciol., 38, 39–44, 2004.

Freitag, J.: Untersuchungen zur Hydrologie des arktischen Meereises - Konsequenzen für den Stofftransport, Ph.D. thesis, Universität Bre-
men, ber. z. Polarforsch., Bd. 325, 1999, 1999.

Freitag, J. and Eicken, H.: Meltwater circulation and permeability of Arctic summer sea ice derived from hydrological field experiments, J.
Glaciol., 49, 349–358, 2003.

Gelb, L., Graham, A. L., Mertz, A. M., and P.H.Koenig.: On the permeability of colloidal gels, Physics of Fluids 31, 31, 021 210,
https://doi.org/https://doi.org/10.1063/1.5054596, 2019.

GeoDict: (Geometric material Models and Computational PreDictions of Material Properties), web: www.geodict.com, 2012-2020.

Gervais, P. C., Dany, F., Bouilloux, L., and Ricciardi, L.: Simulations of filter media performances from microtomography-based computa-
tional domain. Experimental and analytical comparison, Computers and Fluids, 116, 118–128, 2015.

Golden, K. M., Ackley, S. F., and Lytle, V. I.: The percolation phase transition in sea ice, Science, 282, 2238–2241, 1998.

Golden, K. M., Heaton, H. E. A., Miner, J., Pringle, D. J., and Zhu, J.: Thermal evolution of permeability and microstructure in sea ice, Geophys. Res. Lett., 34, L16 501, https://doi.org/10.1029/2007GL030447, 2007.

Griewank, P. J. and Notz, D.: Insights into brine dynamics and sea ice desalination from a 1-D model study of gravity drainage, Journal of Geophysical Research: Oceans, 118, 3370–3386, https://doi.org/10.1002/jgrc.20247, 2013.

Happel, J. and Brenner, J.: Low Reynolds Number Hydrodynamics, M. Nijhoff, Dordrecht, Netherlands, 553 pp., 1986.

Heggli, M., Köchle, B., Matzl, M., Pinzer, B., Riche, F., Steiner, S., Steinfeld, D., and Schneebeli, M.: Measuring snow in 3-D using X-ray tomography: assessment of visualization techniques, Ann. Glaciol., 52, 231–236, 2011.

Henkel, M., Hinrichsen, H., and Lübeck, S.: Non-equlibrium phase transitions. Volume I: Absorbing phase transitions, Springer, 385 pp., 2008.

Hinrichsen, H.: Observation of directed percolation - a class of nonequilibrium phase transitions, Physics, 2, https://doi.org/10.1103/Physics.2.96, 2009.

Kawamura, T.: Studies on preferred growth of sea ice grain, Contri. Inst. Low Temp. Sci., contr. 3120, 1–29, 1988.

Kinney, J. H. and Nichols, M. C.: X-ray tomographic microscopy (XTM) using synchrotron radiation, Annu. Rev. Mater. Sci., 22, 121–152, 1992.

Kovacs, A. and Morey, R. M.: Radar anisotropy of sea ice due to preferred azimuthal orientation of the horizontal c axes of ice crystals, J. Geophys. Res., 83, 6037–6046, 1978.

Krembs, C., Mock, T., and Gradinger, R.: A mesocosm study of physical-biological interactions in artifical sea ice: effects of brine channel surface evolution and brine movement on agal mass, Polar Biol., 24, 356–364, 2001.

Langhorne, P. J. and Robinson, W.: Alignment of crystals in sea ice due to fluid motion, Cold Reg. Sci. Techn., 12, 197–214, 1986.

Lieb-Lappen, R., Golden, E., and Obbard, R.: Metrics for interpreting the microstructure of sea ice using X-ray micro-computed tomography, Cold Reg. Sci. Technol., 138, 24–35, 2017.

Light, B., Maykut, G. A., and Grenfell, T. C.: Effects of temperature on microstructure of first-year Arctic sea ice, J. Geophys. Res., 108, 3051–3066, 2003.

Linden, S., Cheng, L., and Wiegmann, A.: Specialized methods for direct numerical simulations in porous media, Tech. Rep. 2018-01, Math2Market, https://doi.org/10.30423/report.m2m-2018-01, 2018.

Maksym, T. and Jeffries, M. O.: A one-dimensional percolation model of flooding and snow ice formation on Antarctic sea ice, J. Geophys. Res., 105, 26 313–26 331, 2000.

Maus, S.: On Brine Entrapment in Sea Ice: Morphological Stability, Microstructure and Convection, Logos, Berlin, 538 pp., 2007.

Maus, S., Haase, S., Büttner, J., Huthwelker, T., Schwikowski, M., Vähätalo, A., and Enzmann, F.: Ion fractionation in young sea ice from Kongsfjorden, Svalbard, Ann. Glaciol., 52, 301–310, 2011.

Maus, S., Leisinger, S., Matzl, M., Schneebeli, M., and Wiegmann, A.: Modelling oil entrapment in sea ice on the basis of microtomographic images, in: Proceedings - Port and Ocean Engineering under Arctic Conditions, Espoo, Finland., POAC, 10 pp., 2013.

Maus, S., Becker, J., Leisinger, S., Matzl, M., Schneebeli, M., and Wiegmann, A.: Oil saturation of the sea ice pore space, in: Proceedings - Port and Ocean Engineering under Arctic Conditions, Trondheim, Norway, POAC, 12 pp., 2015.

Nield, D. A. and Bejan, A.: Convection in Porous Media, Springer, 2nd edn., 546 pp., 1999.

Obbard, R., Trodermann, G., and Baker, I.: Imaging brine and air inclusions in sea ice using micro-X-ray computed tomography, J Glaciol., 55, 1113–1115, 2009.

Okada, M., Kang, C., and Okiyama, H.: Advances in Cold-Region Thermal Engineering and Sciences, vol. 533 of *Lecture Notes in Physics, LNP*, chap. Permeability of an aqueous solution in a state of partial solidification, pp. 103–112, Springer, 1999.

Ono, N. and Kasai, T.: Surface layer salinity of young sea ice, Ann. Glaciol., 6, 298–299, 1985.

Otsu, N.: A threshold selection method from gray-level histograms, IEEE Transactions on Systems, Man and Cybernetics, SMC-9, 62–66, 1979.

Paterson, M. S.: The equivalent channel model for permeability and resistivity in fluid-saturated rock - a re-appraisal, Mech. of Materials, 2, 345–352, 1983.

Petrich, C., Langhorne, P. J., and Sun, Z. F.: Modelling the interrelationships between permeability, effective porosity and total porosity in sea ice, Cold Reg. Sci. Techn., 44, 131–144, 2006.

Pringle, D. J., Miner, J. E., Eicken, H., and Golden, K. M.: Pore space percolation in sea ice single crystals, J. Geophys. Res., 114, https://doi.org/10.1029/2008JC005145, 2009.

Rees Jones, D. and Grae Worster, M.: A physically based parametrization of gravity dtainage for sea ice modeling, J. Geophys. Res., 119, 5599–5621, https://doi.org/10.1002/2013JC009296, 2014.

Saeki, H., Takeuchi, T., Sakai, M., and Suenaga, E.: Experimental study on the permeability coefficient of sea ice, in: Ice Technology, Proceedings: 1st International Conference, edited by T.K.S. Murthy, J. C. and C.A.Brebia, pp. 237–246, Springer-Verlag, New York, 1986.

Sahimi, M.: Flow phenomena in rocks, Rev. of Mod. Phys., 65, 1393–1534, 1993.

Saito, T. and Ono, N.: Percolation of sea ice. I: Measurement of Kerosine permeability of NaCl ice, Low Temp. Sci., A37, 55–62, 1978.

Schneebeli, M. and Sokratov, S. A.: Tomography of temperature gradient metamorphism of snow and associated changes in heat conductivity, Hydrol. Processes, 18, 3655–3665, 2004.

Stauffer, D. and Aharony, A.: Introduction to Percolation Theory, Taylor & Francis, 2nd edition edn., 1992.

Turner, A. K., Hunke, E. C., and Bitz, C. M.: Two modes of sea-ice gravity drainage: A parameterization for large-scale modeling, Journal of Geophysical Research: Oceans, 118, 2279–2294, 2013.

Vancoppenolle, M., Bitz, C. M., and Fichefet, T.: Summer landfast sea ice desalination at Point Barrow, Alaska: Modeling and observations, Journal of Geophysical Research: Oceans, 112, 2156–2202, https://doi.org/10.1029/2006JC003493, c04022, 2007.

Wakatsuchi, M.: Experiments on the growth of sea ice and the rejection of brine, Low Temp. Sci., A32, 195–205, 1974.

Wakatsuchi, M.: Brine exclusion processes from growing sea ice, Contrib. Inst. Low Temp. Sci., A33, 29–65, 1983.

Weeks, W. F.: On Sea Ice, University of Alaska Press, 2010.

Weissenberger, J., Dieckmann, G., Gradinger, R., and Spindler, M.: Sea ice: A cast technique to examine and analyze brine pockets and channel structure, Limnol. Ocean., 37, 179–183, 1992.

Wells, A., Wettlaufer, J., and Orszag, S. A.: Nonlinear mushy-layer convection with chimneys: stability and optimal solute fluxes, J. Fluid Mech., 716, 203–227, https://doi.org/doi.org/10.1017/jfm.2012.541, 2013.

Wiegmann, A.: Computation of the permeability of porous materials from their microstructure by FFF-Stokes., vol. ITWM-Berichte, 129, Kaiserslautern: Fraunhofer ITWM, 1434-9973, 2007.

Worster, M. G. and Wettlaufer, J. S.: Natural convection, solute trapping, and channel formation during solidification of saltwater, J. Phys. Chem. B, 101, 6132–6136, https://doi.org/S/, 1997.

Zermatten, E., Haussener, S., Schneebeli, M., and Steinfeldt, A.: Tomography-based determination of permeability and Dupui Forchheimer coefficient of characteristic snow samples, J. Glaciol., 47, 811–816, 2011.